



# MgH<sub>2</sub> thin films and nanowires deposited by CVD from a magnesium diamidodiboranate precursor

Laurent Souqui<sup>a,\*</sup>, Christopher M. Caroff<sup>b</sup>, R. Joseph Lastowski<sup>b</sup>, Samyukta Shrivastav<sup>c,d</sup>, Gregory S. Girolami<sup>b</sup>, Jessica A. Krogstad<sup>c,d</sup>, John R. Abelson<sup>c,d</sup>

<sup>a</sup> Department of Chemistry – Ångström laboratory, Uppsala University, Uppsala 752 37, Sweden

<sup>b</sup> School of Chemical Sciences, University of Illinois at Urbana-Champaign, Urbana, IL 61801, USA

<sup>c</sup> Department of Materials Science and Engineering, University of Illinois at Urbana-Champaign, Urbana, IL 61801, USA

<sup>d</sup> Materials Research Laboratory, University of Illinois at Urbana-Champaign, Urbana, IL 61801, USA

## ARTICLE INFO

### Keywords:

Magnesium hydride  
Chemical vapor deposition  
Single-source precursor  
Thin films  
Nanowires  
Low-temperature synthesis  
One-step synthesis

## ABSTRACT

Magnesium hydride, MgH<sub>2</sub>, is deposited by chemical vapor deposition (CVD) at substrate temperatures of 140–300 °C from the newly synthesized magnesium diamidodiboranate precursor, Mg(NMe<sub>2</sub>BH<sub>2</sub>NMe<sub>2</sub>BH<sub>3</sub>)<sub>2</sub>, abbreviated Mg(NBNB)<sub>2</sub>. The resulting films are pure, single-phase MgH<sub>2</sub> as evidenced by X-ray diffraction and Raman spectroscopy. Depending on the growth conditions, the morphology of the deposits can be varied from a granular film to islands to a continuous film with either protruding pillars or nanowires. The deposits are nanocrystalline and consist of pure, polycrystalline α-MgH<sub>2</sub> under all conditions. The formation of MgH<sub>2</sub> from Mg(NBNB)<sub>2</sub> is thought to involve a hydrogen elimination mechanism involving the BH<sub>2</sub> or BH<sub>3</sub> groups.

## 1. Introduction

Magnesium hydride, MgH<sub>2</sub>, is a lightweight ceramic material with three known phases: α-MgH<sub>2</sub>, which has a tetragonal (rutile) structure and is stable at ambient pressure; and β-MgH<sub>2</sub> and γ-MgH<sub>2</sub>, which have cubic and orthorhombic structures, respectively, but are stable only at elevated pressures [1]. The α phase is a dielectric with a band gap of about 5.6 eV [2]. When α-MgH<sub>2</sub> is heated above 410 °C in powder form, it dehydrogenates to form metallic magnesium [3,4]. In part owing to these properties, the α-phase has been extensively studied as a potential material for hydrogen storage [5–12], for switchable windows and mirrors [13,14], electronics [15], and for anti-reflecting passivation layers in photovoltaics [16,17].

Bulk samples of MgH<sub>2</sub> have been obtained by the pyrolysis of diethylmagnesium (Mg(C<sub>2</sub>H<sub>5</sub>)<sub>2</sub>) at 200 °C in high vacuum [18]. In contrast, under similar conditions di-*n*-butylmagnesium (Mg(C<sub>4</sub>H<sub>9</sub>)<sub>2</sub>) produces a mixture of Mg and MgH<sub>2</sub>, and diphenylmagnesium (Mg(C<sub>6</sub>H<sub>5</sub>)<sub>2</sub>) affords only Mg. High-energy ball milling of Mg in H<sub>2</sub> is most often employed to obtain MgH<sub>2</sub> for use as a hydrogen storage material. This route affords MgH<sub>2</sub> with a grain size of tens of nanometers; the high density of grain boundaries and high specific surface area lower the

macroscopic onset temperature for dehydrogenation [19–23]. Additives and alloying can further reduce the temperature required to achieve full dehydrogenation, but at the cost of reduced hydrogen storage capacity. However, the small grains are not stable under cycling: rehydrogenation at elevated temperatures heals defects and coarsens the grain size, thus degrading performance [24,25]. To mitigate coarsening, liquid phase synthesis has been used to afford MgH<sub>2</sub> nanoparticles in a carbon scaffold [26–29], and reactive evaporation under 1–4 MPa H<sub>2</sub> pressure has been used to form MgH<sub>2</sub> nanowires and nanostructures [30–34]. The latter process has sometimes been labelled “hydriding CVD” despite having no characteristics of CVD processes [30–34].

Thin films of MgH<sub>2</sub> have been grown by low-pressure (< 1 atm) hydrogenation of Mg in contact with a Pd layer [2,13,14], by reactive evaporation of Mg in an atomic hydrogen beam [35], and by reactive sputtering of Mg in the presence of an argon-hydrogen plasma [16,17,36,37]. These methods typically afford a mixture of MgH<sub>2</sub> and metallic Mg. Because sputtering and evaporation are line-of-sight techniques, these methods are useful only for applications that involve relatively planar substrates.

To date, no chemical vapor deposition (CVD) method to grow MgH<sub>2</sub> thin films has been described, even though CVD is a desirable method for

\* Corresponding author.

E-mail addresses: [laurent.souqui@kemi.uu.se](mailto:laurent.souqui@kemi.uu.se) (L. Souqui), [christopher.caroff@mcgc.com](mailto:christopher.caroff@mcgc.com) (C.M. Caroff), [lastowski@lanl.gov](mailto:lastowski@lanl.gov) (R.J. Lastowski), [ss101@illinois.edu](mailto:ss101@illinois.edu) (S. Shrivastav), [ggirolam@illinois.edu](mailto:ggirolam@illinois.edu) (G.S. Girolami), [jakrogst@illinois.edu](mailto:jakrogst@illinois.edu) (J.A. Krogstad), [abelson@illinois.edu](mailto:abelson@illinois.edu) (J.R. Abelson).

<https://doi.org/10.1016/j.mtcomm.2025.114615>

Received 12 October 2025; Received in revised form 15 December 2025; Accepted 31 December 2025

Available online 2 January 2026

2352-4928/© 2026 The Author(s). Published by Elsevier Ltd. This is an open access article under the CC BY license (<http://creativecommons.org/licenses/by/4.0/>).

film growth because it is relatively fast and can be scaled to large areas [38]. In addition, if the film's growth rate is limited by surface reactions, then the deposit can be conformal over (and within) complex morphologies and structures [38–44]. We note that conformal coatings of  $\text{MgH}_2$  on suitably nanostructured substrates might be ideally suited for hydrogen storage applications [45].

Here, we report the low-pressure CVD of  $\alpha\text{-MgH}_2$  films at 140–300 °C using a newly synthesized single-source precursor [46], magnesium bis(diamidoborane),  $\text{Mg}(\text{NMe}_2\text{BH}_2\text{NMe}_2\text{BH}_3)_2$ , abbreviated Mg(NBNB)<sub>2</sub>. During the deposition process, each ligand transfers one H atom to the Mg center, most likely from a  $\text{BH}_3$  or  $\text{BH}_2$  group via a hydrogen elimination reaction. The reaction proceeds efficiently to afford phase-pure  $\text{MgH}_2$  plus volatile by-products, as evidenced by X-ray diffraction, Raman spectroscopy, X-ray photoelectron spectroscopy, and Rutherford backscattering spectrometry. Smooth, nanocrystalline films with a thickness up to 60 nm and with optical properties close to those of bulk  $\text{MgH}_2$  can be obtained at short deposition times (< 30 min) and low temperatures (140–200 °C). The crystallite size, which is particularly important for hydrogen desorption kinetics, is reproducibly controlled by varying the precursor flux. At longer deposition times, growth instabilities afford  $\text{MgH}_2$  pillars, whereas increasing the deposition temperature leads to the formation of  $\text{MgH}_2$  nanowires with an average width of ~ 50 nm. These high surface area deposits are potentially of interest in the context of fast, reversible hydrogen storage media.

## 2. Experimental details

### 2.1. Substrate preparation

We use a variety of substrates to facilitate post-growth analysis, as noted in the Results section below. Two aspects were considered: the stability of the oxide and the overlaps between film and substrate in characterization methods, especially Raman. Regarding stability, we previously observed that a different precursor, magnesium dimethylaminodiborane,  $\text{Mg}(\text{DMADB})_2$ , reacts with  $\text{SiO}_2/\text{Si}$  and Au substrates to form  $\text{Mg}_2\text{Si}$  and  $\text{MgAu}$ , respectively [47]. The use of a diffusion barrier is also critical during hydrogen cycling, where metallic Mg can react with the substrate as shown by Le-Quoc et al [36].

The investigated oxides are thin films of  $\text{HfO}_2$ ,  $\text{TiO}_2$ ,  $\text{RuO}_2$ ,  $\text{WO}_3$  deposited on silicon substrates and native  $\text{SiO}_2$ . The synthesis of  $\text{HfO}_2$ ,  $\text{TiO}_2$ ,  $\text{RuO}_2$ , and  $\text{WO}_3$  is as follows:

- $\text{HfO}_2$ : after degreasing of the substrate in acetone and in isopropanol in an ultrasonic bath for 5 min each,  $\text{HfO}_2$  is deposited by atomic layer deposition (ALD, Savannah S100 Cambridge Nanotech) on native  $\text{SiO}_2$  at 120 °C from tetrakis(dimethylamido)hafnium,  $\text{Hf}(\text{N}(\text{CH}_3)_2)_4$ , and  $\text{H}_2\text{O}$  to a thickness of 8.4–9.0 nm (85 ALD cycles).
- $\text{TiO}_2$ : after degreasing of the substrate in acetone and in isopropanol in an ultrasonic bath for 5 min each,  $\text{TiO}_2$  is deposited by ALD on native  $\text{SiO}_2$  at 200 °C from tetrakis(dimethylamido)titanium,  $\text{Ti}(\text{N}(\text{CH}_3)_2)_4$ , and  $\text{H}_2\text{O}$  to a thickness of 14 nm (300 ALD cycles).
- $\text{RuO}_2$ : after degreasing of the substrate in acetone and in isopropanol in an ultrasonic bath for 5 min each, Ru is deposited by e-beam evaporation on a silicon substrate with a 300-nm-thick thermal silicon oxide to a thickness of 5–6 nm followed by exposure to air at room temperature.
- $\text{WO}_3$ : after degreasing of the substrate in acetone and in isopropanol in an ultrasonic bath for 5 min each, W is deposited by e-beam evaporation on a silicon substrate with a 300-nm-thick thermal silicon oxide to a thickness of 50 nm followed by annealing at 400 °C in  $\text{O}_2$  for 3 h.

Most of the experiments in the present work use Si wafers coated with ALD  $\text{HfO}_2$  because we find that the latter material remains unaffected by the deposition process (Figure S6) and acts as a diffusion barrier to prevent reaction of the precursor with the underlying

substrate. It also is and remains amorphous at the deposition temperatures used for  $\text{MgH}_2$  which facilitates the XRD analysis, unlike  $\text{WO}_3$  and  $\text{RuO}_2$  that are polycrystalline and nanocrystalline, respectively.

Finally, we realize using Raman spectroscopy that the vibrational spectrum of the silicon substrate overlaps with the one of  $\text{MgH}_2$ . To be able to measure the Raman spectrum of the films, a multilayer  $\text{HfO}_2/\text{Au}/\text{Cr}/\text{SiO}_2/\text{Si}(100)$  is used. First, a 5-nm-thick Cr adhesion layer is deposited on native  $\text{SiO}_2$  by e-beam evaporation. A 54-nm-thick layer of Au is then deposited by e-beam evaporation to act as a mirror and cut off the signal from the substrate. Finally,  $\text{HfO}_2$  is then deposited as previously described to prevent the formation of the intermetallic  $\text{MgAu}$  during the deposition of  $\text{MgH}_2$  and for consistency.

### 2.2. $\text{MgH}_2$ deposition

Films are deposited in a turbopumped, load-locked high vacuum chamber (base pressure <  $4.5 \times 10^{-7}$  Torr) described elsewhere [48,49]. The  $\text{Mg}(\text{NBNB})_2$  precursor [46] is heated in a water bath to 40–60 °C, which is sufficient to melt it without decomposition. To prevent premature condensation of the precursor, the delivery line is heated to a temperature that is 10 °C above that of the precursor bath. No carrier gas is used. The precursor is delivered to the chamber through a 4.2-mm inner diameter stainless steel tube pointing towards, and 7 cm away from, the substrate. The substrate is maintained at 140–300 °C by a radiative heater located on its underside. The partial pressure of the precursor under dynamic pumping ranges from 0.004 to 0.060 mTorr. Due to the forward-directed injection of precursor, however, the incident flux on the substrate is estimated to be several times larger than the isotropic flux corresponding to the partial pressure in the room-temperature chamber.

The deposition process is monitored *in situ* by spectroscopic ellipsometry between 0.75 and 4.0 eV at an incidence angle of 70° with respect to the sample normal. After the onset of precursor flow into the chamber, the ellipsometry parameters are constant over times ranging from 0.5 to 30 min, depending on the growth conditions, owing to a slow rate of film nucleation. During this period, the optical parameters of the film cannot be modeled due to the unknown surface geometry (e.g., formation and coalescence of islands) [50]. After the nucleation period, the ellipsometry parameters begin to change rapidly as steady-state film growth commences. The surface can then be modeled as a thin dielectric on top of the substrate. In this work, we report the duration of film growth as the time between the onset of steady-state growth as detected by ellipsometry and the cessation of precursor flow.

The substrates are stored in air in polypropylene wafer carriers. Before being loaded into the chamber, the substrates are cut into  $10 \times 12 \text{ mm}^2$  pieces, degreased in an ultrasonic bath in acetone and in isopropanol for 5 min each, exposed to UV/ $\text{O}_3$  cleaning for 10 min and loaded into the chamber. Once the base pressure of  $4.5 \times 10^{-7}$  Torr is reached, the substrates are radiatively heated to the growth temperature, as measured with an exposed thermocouple in contact with the sample surface. The substrates are kept at the growth temperature for 10 min before the precursor flow starts.

Relative to a reference thermocouple that is located deep within the radiative heating assembly, the temperature reading of the sample thermocouple progressively shifts to higher temperatures as successive deposition runs are carried out; the offset can be as large as 70 °C. Heating the sample stage (and thus annealing the thermocouple) to > 450 °C, however, restores the agreement between the substrate and reference thermocouples. We attribute the temperature shift to the formation of a  $\text{MgH}_2$  or Mg coating on the exposed thermocouple; annealing the thermocouple evaporates the deposit. Periodically, we also check the temperature of the sample stage using a reference CVD experiment. We flow tetrakis(dimethylamido)vanadium, whose growth onset temperature is 160–167 °C [51], and increase the substrate temperature by steps of 10 °C; the actual temperature of the substrate is assigned to be 160 °C for the lowest temperature setting at which the

ellipsometry parameter  $\Delta$  changes after 15 min. Owing to the uncertainties in the substrate temperature, however, we give only qualitative assessments of how the reaction kinetics change as a function of temperature.

### 2.3. Thin film characterization

The phase of the films is investigated by X-ray diffraction (XRD) as well as  $\mu$ -Raman spectroscopy. The X-ray diffractograms are recorded on a Bruker D8 ADVANCE Plus diffractometer equipped with a Cu X-ray anode, a Göbel mirror to obtain a parallel beam, a 2-mm divergence slit on the primary side,  $2.5^\circ$  Soller slits on the secondary side, and an EIGER2 R 500 K detector. A sapphire single-crystal crystal (which gives a low XRD background) is used as a sample holder. The incident angle  $\alpha$  is fixed at  $1^\circ$  for glancing incidence measurements (GI-XRD).  $\mu$ -Raman spectroscopy is performed on a film deposited on  $\text{HfO}_2/\text{Au}/\text{Cr}$ -coated substrates with a confocal Raman microscope (Nanophoton Raman 11) that employs a 531.9 nm excitation laser at 0.10 mW, objective  $\times 100$  and 2400 line/mm grating. The gold underlayer is used to block Raman scattering from the Si substrate, which otherwise interferes with the  $\text{MgH}_2$  Raman bands at  $300\text{ cm}^{-1}$  and  $950\text{ cm}^{-1}$  (at room temperature and with excitation wavelength of 488 nm) [4,52–54]. The spectrum is obtained by averaging thirty 12-second scans over an area of  $864\text{ }\mu\text{m}^2$ . Spikes due to cosmic rays are removed manually.

X-ray photoelectron spectroscopy (XPS, Kratos Analytical AXIS) and Rutherford backscattering spectrometry (RBS, NEC Pelletron accelerator) are used to assess the composition of the films. For XPS, the X-ray anode (monochromatic Al  $K\alpha$  radiation, 1486.6 eV) was operated at 210 W at a base pressure of  $5.9 \times 10^{-9}$  Torr. The binding energy scale was calibrated to the Au 4  $f_{7/2}$  core-level peak at 84.0 eV and the Cu  $2p_{3/2}$  peak at 932.6 eV. No sputter cleaning procedure is used. Sample charging is compensated with a flood gun, and adventitious carbon is set to 284.8 eV. The CasaXPS software (version 2.3.13) is used to analyze the XPS data. Atomic ratios are determined from the XPS peak intensities by factoring in the relative sensitivity coefficients. For RBS, the incident beam is 2.03 MeV  $^4\text{He}^+$  incident at  $22.5^\circ$  to the sample normal, the detector angle is  $52.5^\circ$  with respect to the sample normal, and the scattering angle is  $150^\circ$ . The energy scale is calibrated with two reference samples: Pt/Mn/Si and Au/Cu/Si. The RBS spectra are fitted by using the SIMNRA software (version 7.03).

The morphology of the deposited films is characterized by scanning electron microscopy (SEM, Hitachi S-4800) and an in-lens detector. The accelerating voltage is 10 kV. For transmission electron microscopy (TEM, JEOL 2010 LaB6), samples are scraped with a blade onto a TEM grid consisting of a carbon film on 200 mesh Cu grid (Ted Pella Inc.) and imaging is carried out with an accelerating voltage of 200 kV. The optical properties and thickness of the continuous granular films are measured *ex situ* by variable angle spectroscopic ellipsometry (VASE, J. A. Woollam instrument) in the range 0.95–4.13 eV. The measurements are performed at incident angles of  $50^\circ$ ,  $60^\circ$ , and  $70^\circ$ . The use of variable angles of incidence affords an unambiguous deconvolution of the optical thickness into the physical thickness and index of refraction of each layer. Both *in situ* and variable-angle spectroscopic ellipsometry data are analyzed with the CompleteEASE software (version 5.04).

## 3. Results and discussion

### 3.1. Morphology

Depending on the growth conditions, the magnesium diamidodiboranate precursor  $\text{Mg}(\text{NBnB})_2$  affords films of significantly different morphologies, including granular films, pillars, and nanowires.

For substrate temperatures of 140–200  $^\circ\text{C}$ , continuous granular films with grain sizes of up to  $\sim 60\text{ nm}$  are observed for growth times  $< 30\text{ min}$  (Fig. 1). The morphology and grain sizes at a given thickness are independent of the precursor partial pressure up to the experimental

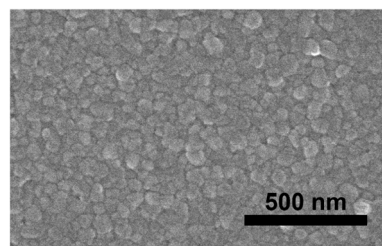


Fig. 1. Planar SEM of a continuous  $\text{MgH}_2$  film with a granular morphology deposited at 0.010 mTorr at 200  $^\circ\text{C}$  for 21.5 min on  $\text{HfO}_2/\text{Si}$ .

maximum of 0.60 mTorr, although the growth rate increases linearly with pressure (Fig. 2). In this same temperature range, however, the morphology becomes dominated by pillars if the growth time is longer than 30 min. For example, after 120 min at 200  $^\circ\text{C}$  and a precursor pressure of 0.010 mTorr, pillars of length 260–280 nm protrude from a continuous, 60 nm thick  $\text{MgH}_2$  film (Fig. 3). The width of the pillars decreases from 100 nm at the base to 60 nm at the top. This morphology is consistent with morphological instability models used to describe protrusions observed in thermal CVD of polycrystalline Si [55–57].

At higher temperatures, the morphology for growth times  $< 30\text{ min}$  evolves from the continuous granular films seen at 200  $^\circ\text{C}$  to a percolated network of islands at 225  $^\circ\text{C}$  (Fig. 4(a)) to separate elongated islands at 280  $^\circ\text{C}$  (Fig. 4(b)). At these higher growth temperatures, a continuous faceted film with protruding nanowires is eventually formed at longer growth times (Fig. 5). From a mechanistic perspective, faceting requires significant anisotropic attachment of adspecies during growth, which may contribute to vapor-solid growth of nanowires [58–61].

Increasing the deposition time results in increases in both the nanowire length and density (as can be seen by comparing Fig. 4 with Fig. 5). Some of the nanowires appear to originate from a broad pillar, but such pillars are not seen at shorter deposition times (Fig. 4(b)): the wires emerge between crystallites and do not have a broadened base. We interpret the pillar-like base of the nanowires in Fig. 5 as evidence of lateral growth of the wire itself, rather than growth from a pre-existing pillar. Furthermore, Fig. 5 suggests that the nanowires have a rectangular cross-section like those of nanoribbons and nanobelts of tetragonal materials such as  $\alpha$ -t B [62],  $\text{SnO}_2$  [63],  $\text{WO}_3$  [64], and  $\text{Ru}_x\text{Ti}_{(1-x)}\text{O}_2$  [65]. Combining SEM and TEM (Fig. 6) we find that the nanowires grown at 243  $^\circ\text{C}$  for 109 min are about  $3.5\text{ }\mu\text{m}$  long and 50 nm wide. For applications in hydrogen storage, a diameter of 50 nm is small enough to improve the kinetics of hydrogen absorption and desorption [68], although smaller dimensions are required to obtain the lowest possible

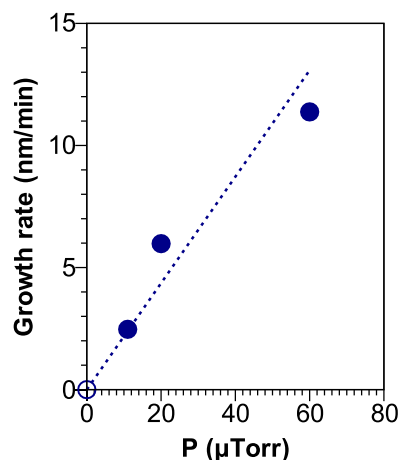
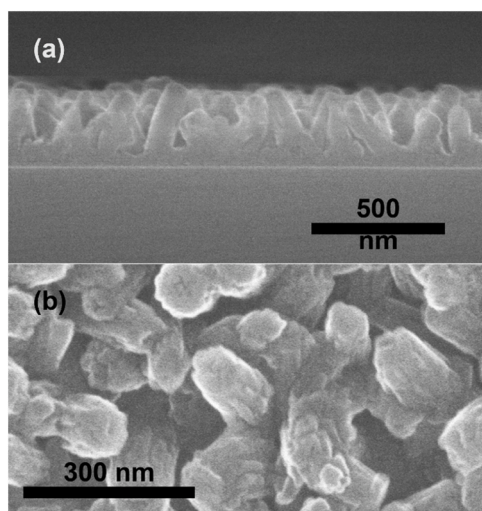
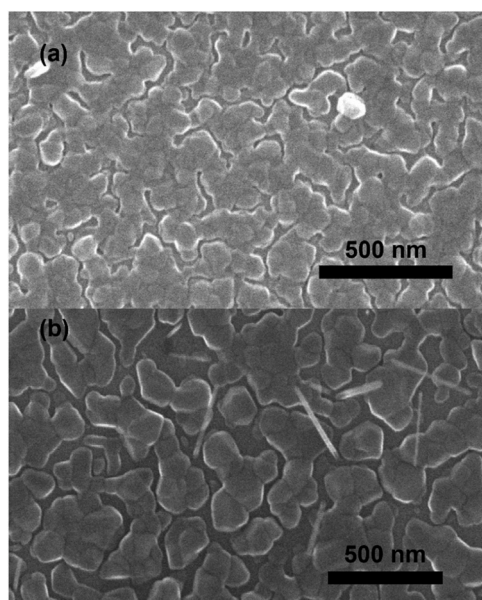


Fig. 2. Influence of  $\text{Mg}(\text{NBnB})_2$  pressure on the growth rate of  $\text{MgH}_2$  at 200  $^\circ\text{C}$  on  $\text{HfO}_2/\text{Si}$ . Solid circles are experimental data obtained from VASE, the open circle at 0 mTorr is trivial.



**Fig. 3.** (a) Cross-sectional and (b) plan-view SEM of a  $\text{MgH}_2$  film deposited on  $\text{HfO}_2/\text{Si}$  at  $200^\circ\text{C}$  over a total deposition time of 120 min, revealing a pillar-like morphology.



**Fig. 4.** Plan-view SEM of  $\text{MgH}_2$  thin films deposited on  $\text{HfO}_2/\text{Si}$  at 0.010 mTorr at (a)  $225^\circ\text{C}$  for 17 min revealing the percolated network of islands and (b)  $280^\circ\text{C}$  for 24 min revealing disconnected, elongated structure with nanowires growing between them.

dehydrogenation temperatures [69,70].

### 3.2. Phase analysis and microstructure

The Raman spectrum of a film deposited at  $215^\circ\text{C}$  for 24 min (Fig. 7) exhibits bands at  $957\text{ cm}^{-1}$  and  $1280\text{ cm}^{-1}$ , which are assigned to the  $E_g$  and  $A_{1g}$  modes of  $\text{MgH}_2$ , respectively, as reported in earlier studies [4, 52–54]. The bands are broadened and slightly blue-shifted compared to those seen for coarser powders and thicker films; these differences could be due to a smaller grain size and/or compressive stress [71,72]. The broad feature near  $1200\text{ cm}^{-1}$  has previously been assigned to two-phonon second-order processes in  $\text{MgH}_2$ .<sup>4</sup>

XRD shows that the only crystalline phase deposited from the thermal decomposition of  $\text{Mg}(\text{NBNB})_2$  on  $\text{HfO}_2/\text{Si}$  is  $\alpha\text{-MgH}_2$  (PDF 00–012–0697; tetragonal, space group  $P4_2/mnm$ ) [73] regardless of the

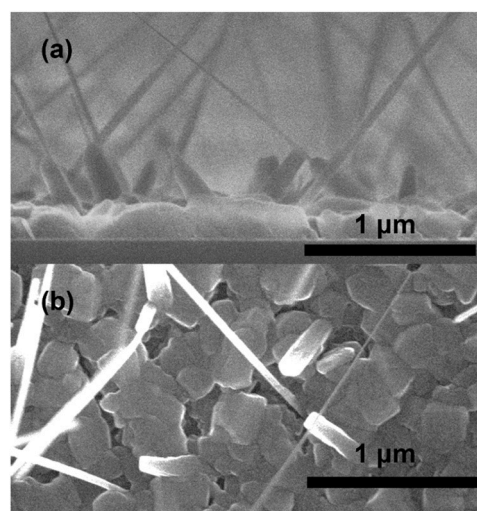


**Fig. 5.** (a) cross-sectional and (b) plan-view SEM of a  $\text{MgH}_2$  film deposited on  $\text{HfO}_2/\text{Si}$  at  $243^\circ\text{C}$  for 109 min. The  $\text{MgH}_2$  film is faceted and coalescing around nanowires with a broadened base. The section of the nanowires appears to be rectangular.

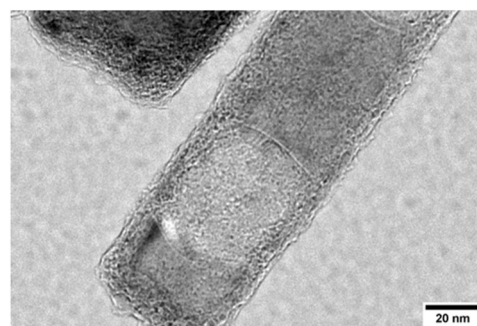


**Fig. 6.** TEM images of  $\text{MgH}_2$  nanowires. The lighter rectangle-shaped region within the wire is due to electron beam damage caused by an attempt to collect diffraction data. Most likely this change reflects dehydrogenation of the  $\text{MgH}_2$ , as has been previously reported [66,67].

morphology of the films (Figures 8 and S1 for pillars, Fig. 9 for planar films, Figure S2 for percolated films with nanowires). The relative intensities of the low index peaks indicate that there is some degree of preferred orientation (see below). Films deposited at higher precursor pressures give broader X-ray diffraction peaks, which we interpret as a reduction in the size of coherently diffracting domains. Application of the Scherrer equation gives crystalline domain sizes of between 6 and 15 nm (hence smaller than the grains observed with SEM), but these values are lower limits owing to the non-Lorentzian line shapes and the possibility of film stress [74,75].

$2\theta/\omega$  diffractograms of the film with nanopillars (Figure S1) show a strong (101) peak and weak (110) and (211) peaks. The relative intensities can be simulated by calculating the powder diffraction pattern of  $\text{MgH}_2$  with a March-Dollase factor arbitrarily set to 0.5 (Figure S3), corresponding to a random powder in which 37.7 % of the crystallites have a preferred (002) and (101) orientation (Figure S3(b) and S3(c) respectively) [76,77]. Surface energy considerations cannot explain either of these preferred orientations, the low energy surface of the  $\text{MgH}_2$  crystal being the (110) plane [78,79]. The preference for a (002) texture can be explained from the symmetry of the crystal (c-axis) as sometimes seen in other materials with a tetragonal structure (rutile  $\text{Ru}_x\text{Ti}_{(1-x)}\text{O}_2$  [65],  $\alpha\text{-t B}$  [62],  $\text{t-WO}_3$  [64]). A (101) texture could be related to the preference of  $\text{MgH}_2$  1D-nanostructures to grow in the [101] direction (and its symmetry equivalent directions) [30,34]. As

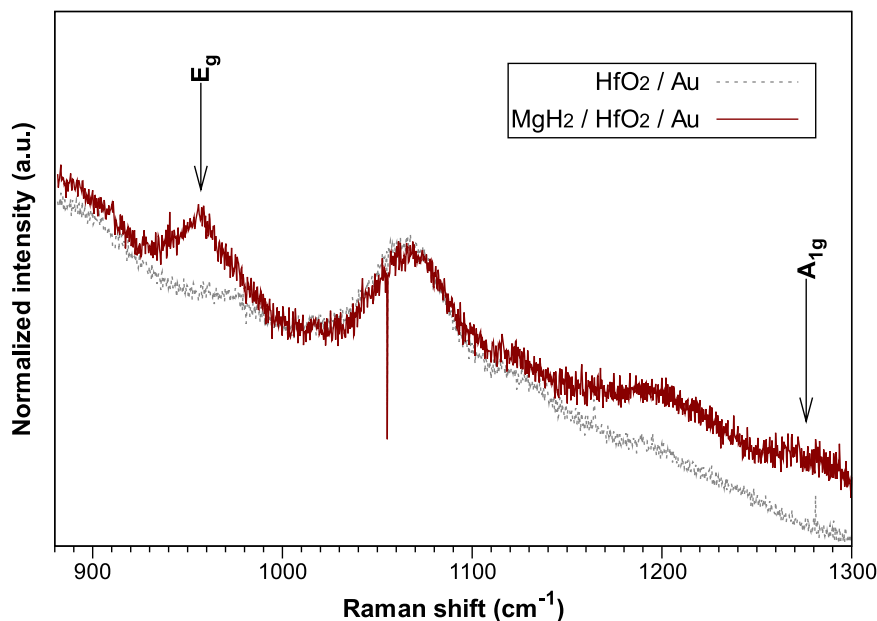


Fig. 7. Raman spectra of an MgH<sub>2</sub> thin film deposited on HfO<sub>2</sub>/Au at 215 °C for 24 min (red solid curve) and of the bare substrate (grey dotted curve). The E<sub>g</sub> and A<sub>1g</sub> modes characteristic of MgH<sub>2</sub> are indicated with black arrows. The broad feature near 1200 cm<sup>-1</sup> is due to two-phonon second-order processes in MgH<sub>2</sub>.

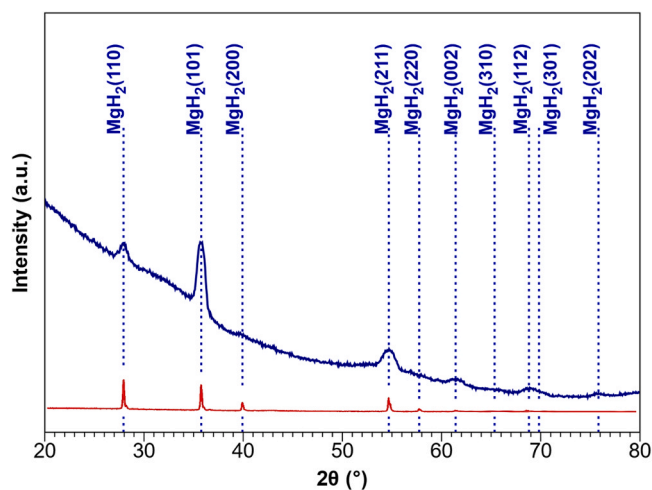


Fig. 8. GI-XRD diffractogram of 270-nm-long MgH<sub>2</sub> pillars on a 60-nm MgH<sub>2</sub> film deposited on HfO<sub>2</sub>/Si at 200 °C for 120 min. The broad background features that extend from around 28–38° and 50–60° originate from the amorphous HfO<sub>2</sub>. The red trace at the bottom is the diffraction pattern seen for a non-oriented sample of α-MgH<sub>2</sub> [95].

Saita *et al.* pointed out, Mg and H atoms form alternating planes perpendicular to the [101] direction [30]. The significant charge transfer of up to 0.8 e to each H atom in MgH<sub>2</sub> therefore makes the [101] direction a polar axis; due to charge balance, this becomes the easy axis for growth, as it is for SnO<sub>2</sub> in the rutile structure, and many 1D-nanostructures of group 13–15 (III-V) or group 12–16 (II-VI) semiconductors [63,80–82].

The 2θ/ω diffractogram (Figure S2) of the percolated films with nanowires deposited at higher temperatures (morphology in Fig. 4) allows us to probe the orientation of the faceted film because, unlike the pillars that comprise most of the film, the nanowires contribute very little to the overall diffraction intensity due to their small aggregate volume. For the faceted films, we find that the (110) peak is strong, whereas the (101), (200), and (211) peaks are weak. These relative intensities match the calculated pattern in Figure S3(d) for a (110) texture;

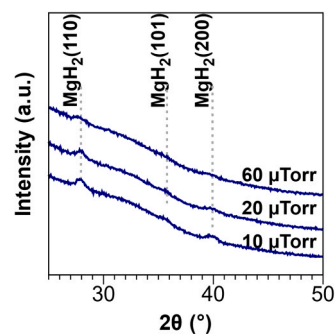


Fig. 9. Influence of the precursor pressure on the breadth of the peaks recorded with GI-XRD of planar MgH<sub>2</sub> thin films deposited on HfO<sub>2</sub>/Si at 200 °C. The thickness of the film deposited at 10 μTorr is 44 nm (average growth rate 2.5 nm/min), at 20 μTorr is 47 nm (6.0 nm/min), and for 60 μTorr is 37 nm (11.4 nm/min).

the (110) planes are the low energy surface of the MgH<sub>2</sub> crystal [78,79]. Thus, the pillars and the faceted films have different orientations.

### 3.3. Composition

At the early stages of film growth (i.e., just after the transition from nucleation to steady-state growth as defined in the previous section), XPS measurements grown on a variety of oxide surfaces show a strong Mg 1s peak at 1303 ± 0.3 eV (e.g., Fig. 10 (c) for a film grown on HfO<sub>2</sub>) consistent with the presence of MgH<sub>2</sub>. Milcius *et al.* [83]. suggested that XPS cannot differentiate magnesium oxides, hydroxides, and hydrides, although more recent work suggests that the binding energy of MgH<sub>2</sub> is about 0.6 eV smaller than that of MgO [84], and about 0.6 eV larger than that of metallic Mg [84].

For these early-stage films grown on RuO<sub>2</sub>, WO<sub>3</sub>, or native SiO<sub>2</sub>, the XPS spectra show no detectable amounts of nitrogen or boron. Similar experiments performed on HfO<sub>2</sub> show no nitrogen (Fig. 10 (a)) but boron is present in amounts close to the detection limit (Fig. 10 (b)), corresponding to a B/Mg atomic ratio of 0.03. On TiO<sub>2</sub>, small amounts of both boron and nitrogen are detected (B/Mg = 0.04 and N/Mg = 0.05) (Figure S5); the nitrogen peaks at 398.7 and 406.2 eV correspond to

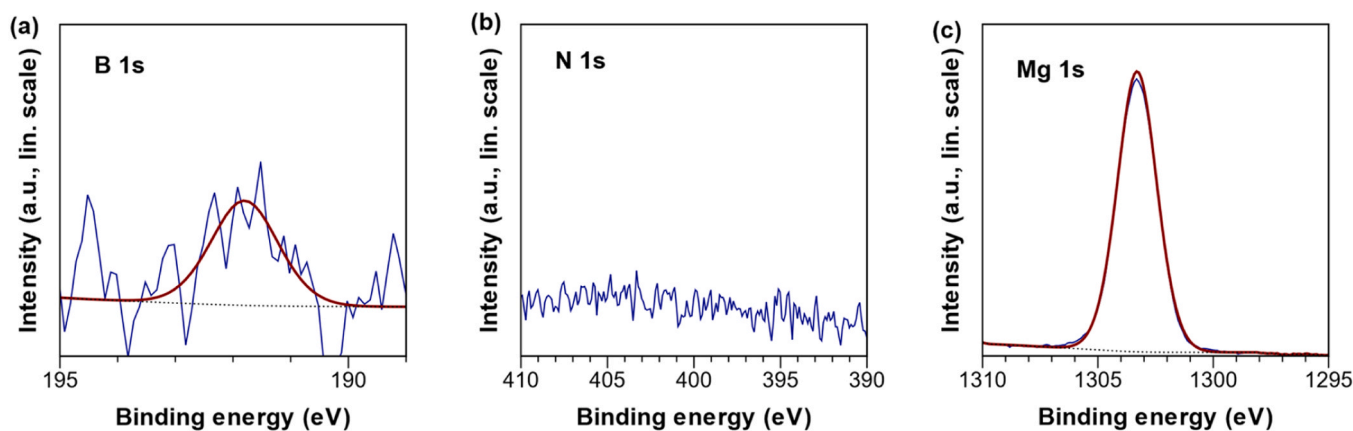


Fig. 10. High resolution XPS core spectra of (a) B 1 s, (b) N 1 s, and (c) Mg 1 s for a sample grown on HfO<sub>2</sub> at 270 °C. The blue solid line is the raw spectrum, the red solid line is the fit (Gaussian-Lorentzian product, 30 % Lorentzian) and the grey dotted line is the (Tougaard) background.

organic and oxidized nitrogen, respectively.

These results suggest that conversion of Mg(NBNB)<sub>2</sub> to MgH<sub>2</sub> occurs cleanly with loss of all or nearly all of the nitrogen and boron. The presence of small amounts of these elements may be due to substrate effects. On HfO<sub>2</sub> and TiO<sub>2</sub>, the B 1 s binding energy is 191.8 and 191.7 eV, respectively, characteristic of boron oxides. On electronegativity grounds, the borane groups in the NBNB ligands are more likely to react with basic oxides such as TiO<sub>2</sub> and HfO<sub>2</sub> than with acidic oxides such as SiO<sub>2</sub>, RuO<sub>2</sub>, and WO<sub>3</sub>.

Because of the low sensitivity of RBS for light elements, we carried out measurements on the thickest films, which have a nanopillar morphology. No nitrogen, boron, or carbon could be detected in the film by RBS (Figure S7). This result is consistent with the XPS results (although the RBS detection limit for light elements is at the few percent level). The small amount of oxygen is ascribed to surface oxidation when the samples are exposed to air.

The RBS spectrum of a film deposited on HfO<sub>2</sub>/Si at 200 °C for 120 min clearly shows the presence of Mg. The peak intensity and width can be fit well if the film is assumed to be MgH<sub>2</sub> (Fig. 11 (b) and S7 (b)); in contrast, efforts to fit the peak to elemental magnesium always result in an overestimation of the peak height (Fig. 11 (a) and S7 (a)). The reason for the better fit is that hydrogen atoms significantly increase the energy loss rate of the He ions, so that the RBS peak for Mg in MgH<sub>2</sub> is lower in height and greater in width.<sup>1</sup> An even better fit can be obtained by assuming that a small amount of oxygen is present, and by accounting for the roughness of the film using a gamma distribution function (Fig. 11 (c) and S7 (c)) [86]. The best fit results are a composition of 27. (7) at% Mg, 67.(0) at% H and 5.(3) at% O, and a gamma distribution [86] with a FWHM of  $775 \times 10^{15}$  atoms/cm<sup>2</sup>. This latter value corresponds to a standard deviation of the height distribution of  $\sigma = 329 \times 10^{15}$  atoms/cm<sup>2</sup>. The average thickness of the films is  $d = 1770 \times 10^{15}$  atoms/cm<sup>2</sup>, giving  $\sigma/d = 0.18$ .

<sup>1</sup> To explain the strong effect of H, we note that stopping power for <sup>4</sup>He ions depends not only on the atomic numbers of the target elements, but also on the spatial distribution of the electron density. The stopping power is therefore relatively large for light elements: for <sup>4</sup>He ions at 2 MeV, the stopping power of  $7.46 \times 10^{-15}$  eV cm<sup>2</sup> for H (Z = 1) is only a factor of 5.9 less than the value of  $44.10 \times 10^{-15}$  eV cm<sup>2</sup> for Mg (Z = 12) [85]. Using Bragg's rule, the stopping power for pure MgH<sub>2</sub> is then  $19.67 \times 10^{-15}$  eV cm<sup>2</sup>, therefore  $59.60 \times 10^{-15}$  eV cm<sup>2</sup> per Mg atom. We neglect the further complication that MgH<sub>2</sub> is partially ionic, which modifies the electron distribution and thus slightly modifies the stopping power.

### 3.4. Optical properties

MgH<sub>2</sub> thin films have often been explored for optical applications, namely switchable windows and mirrors [13,14] and anti-reflecting passivation layers in photovoltaics [16,17]. For a planar MgH<sub>2</sub> film grown under conditions similar to the film described in Fig. 1, the dielectric function was obtained by fitting the variable angle spectroscopic ellipsometer (VASE) data to a general oscillator model (Fig. 12(a, b)). The imaginary part  $\epsilon_2$  of the dielectric function is fit using two Gaussians at 3.1 and 4.1 eV and the real part  $\epsilon_1$  is adjusted with parameters  $\epsilon_\infty$ , IR pole, and UV pole (Table 1). The resulting absorption coefficient  $\alpha$  (Fig. 12(c)) in the range 0.95–4.13 eV gives a plot whose shape is similar to the one reported by Westerwaal *et al.* for films of MgH<sub>2</sub> deposited by reactive evaporation, but the values of  $\alpha$  are an order of magnitude smaller and the spectrum lacks the absorption below 2 eV attributed to Mg clusters [35]. Conversely, the imaginary part of the dielectric function,  $\epsilon_2$ , reported by Isidorsson *et al.* for hydrogenated magnesium is essentially zero up to 3 eV [2].

From this comparison, we suggest that the two Gaussian contributions may originate from point defects such as H vacancies, because they are expected to form more easily under vacuum growth conditions than under high H<sub>2</sub> pressures, and because such vacancies are expected to form deep localized states within the band gap [15,87,88]. Note that the IR and UV poles are used to model the dispersion due to strong absorption under and above the measured range, respectively. Little interpretation can be based on the IR pole because the only parameter is its amplitude. In contrast, we found that a UV pole with an energy of 5.56 eV is necessary to fit the dielectric function. This energy value is comparable to the bandgap of MgH<sub>2</sub> (reported in other works as 5.6 eV [2], 5.41–5.55 eV [35], 5.8 eV [78,79], and 5.16 eV<sup>69</sup>), consistent with our model.

The refractive index ( $n$ ,  $k$ ) of MgH<sub>2</sub> has typically been measured at a single wavelength (2.1 eV), rather than over a range of wavelengths. We obtain refractive index values ( $n$ ,  $k$ ) of (1.72,  $4.5 \times 10^{-3}$ ) at 2.1 eV which are slightly lower compared with the values of (1.94,  $7.6 \times 10^{-3}$ ) [2,73] for bulk MgH<sub>2</sub> at the same wavelength (Figure S8). We deduce that our CVD films are less dense than films obtained by hydrogenation of magnesium under hundreds of atmospheres of H<sub>2</sub>. Additionally, the presence of oxygen could also lower the refractive index, the latter being lower for magnesium oxide ( $\approx 1.7$  [89,90]) and magnesium hydroxide ( $\approx 1.6$  [91]).

### 3.5. Proposed reaction mechanism

The conversion of Mg(NBNB)<sub>2</sub> to MgH<sub>2</sub> involves the transfer of two hydrogen atoms from the ligands to the magnesium center. We have not

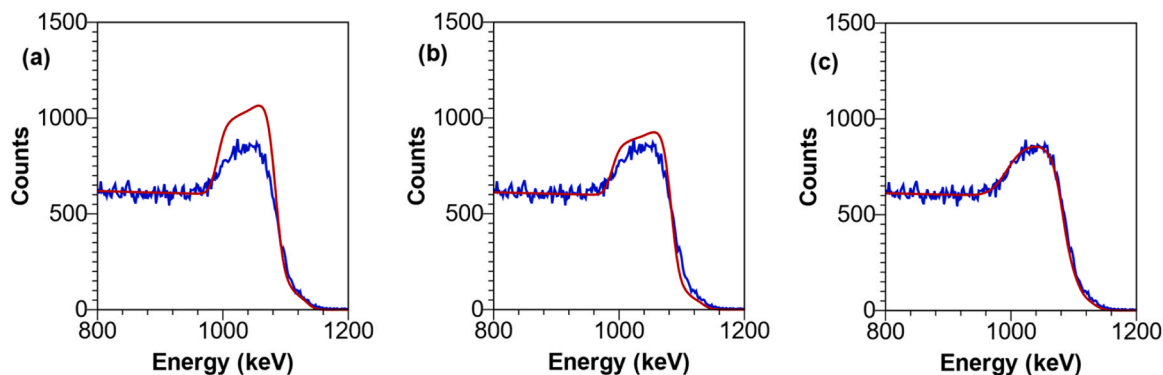


**Fig. 11.** Experimental RBS spectrum (blue solid line) of a MgH<sub>2</sub> film deposited on HfO<sub>2</sub>/Si at 200 °C for 120 min, and simulated spectrum (red solid line): (a) assuming a pure, smooth Mg film gives a poor fit; (b) assuming a pure, smooth MgH<sub>2</sub> film is closer to the experimental data; and (c) including roughness and oxygen contamination affords a perfect fit; see text for details.

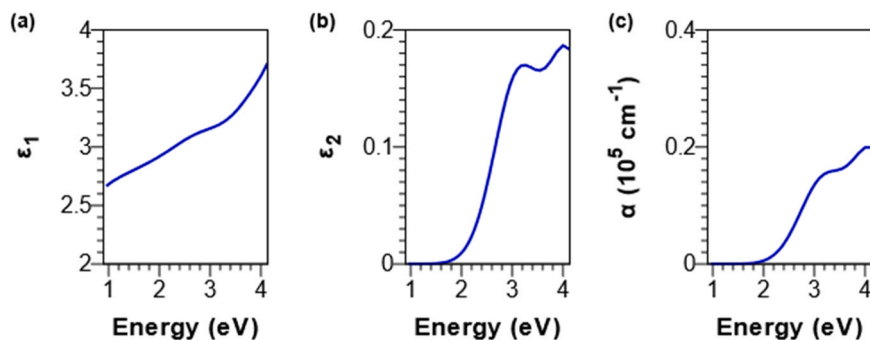


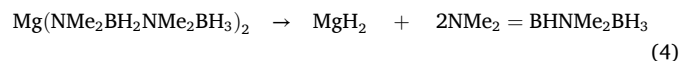
**Fig. 12.** Optical properties of a 35-nm thin film deposited at 180 °C: (a) real part of the dielectric function  $\epsilon_1$ , (b) imaginary part of the dielectric function  $\epsilon_2$ , and (c) absorption coefficient  $\alpha$ .

**Table 1**

Parameters used to fit the dielectric function of a 35-nm MgH<sub>2</sub> thin film deposited at 180 °C with a general oscillator model.

Component	Amplitude	Energy (eV)	FWHM (eV)
Gaussian 1	0.161	3.13	1.12
Gaussian 2	0.167	4.13	0.94
$\epsilon_\infty$	1.83	-	-
IR pole	0.128	-	-
UV pole	27.0	5.56	-

determined experimentally whether the hydrogen elimination reaction involves the BH<sub>2</sub> groups (Eq. 4) or the BH<sub>3</sub> groups (Eq. 5):



where NMe<sub>2</sub>=BHNMe<sub>2</sub> BH<sub>3</sub> is the borane adduct of a known diaminoborane BH(NMe<sub>2</sub>)<sub>2</sub> [92], and (H<sub>2</sub>BNMe<sub>2</sub>)<sub>2</sub> is a known [93,94] cyclic compound analogous to cyclobutane. Specific isotopic labeling of just the BH<sub>2</sub> group or just the BH<sub>3</sub> group with <sup>11</sup>B or <sup>2</sup>H is not possible for the synthetic route we use to make the NBNB ligand.

The NBNB ligands are isoelectronic and isosteric with 1,1,3,3-tetra-methyl-substituted *n*-butyl groups, -CMe<sub>2</sub>CH<sub>2</sub>CMe<sub>2</sub>CH<sub>3</sub>; Eqs. (4) and (5) are analogous to  $\beta$ -hydrogen and  $\delta$ -hydrogen elimination processes, respectively (although in the NBNB ligand, the BH<sub>3</sub> hydrogen atoms are also  $\alpha$  to the Mg center). Both mechanisms seem reasonable to us. For comparison,  $\beta$ -hydrogen elimination the pathway responsible for the formation of MgH<sub>2</sub> by bulk pyrolysis of diethylmagnesium (Mg(CH<sub>2</sub>CH<sub>3</sub>)<sub>2</sub>) and di-*n*-butylmagnesium (Mg(CH<sub>2</sub>CH<sub>2</sub>CH<sub>2</sub>CH<sub>3</sub>)<sub>2</sub>) [18].

Neither of these magnesium alkyls is volatile, however, and so they are unsuitable as CVD precursors.

#### 4. Conclusions

We demonstrate the single-source chemical vapor deposition of MgH<sub>2</sub> thin films using the novel diaminodiborane precursor Mg(NBNB)<sub>2</sub> in the temperature range 140–300 °C. Raman spectroscopy and XRD confirm that the deposited films are pure, single-phase  $\alpha$ -MgH<sub>2</sub> and do not contain Mg clusters as often observed in films obtained by non-CVD methods. From the low concentrations of heteroatoms (B, C, N) and other impurities in the films, we conclude that the decomposition of Mg(NBNB)<sub>2</sub> into MgH<sub>2</sub> occurs cleanly by forming one or more volatile by-products by a hydrogen-elimination mechanism involving the BH<sub>2</sub> or BH<sub>3</sub> groups.

At deposition temperatures below 200 °C, thin continuous films with a granular morphology are obtained at short deposition times. The optical absorption of these films is low in the visible region (i.e., between 1 and 2 eV) but increases at higher energies. The refractive index at 2.1 eV is smaller than that of bulk material. At longer deposition times, pillars develop with a preferential orientation normal to the substrate along the polar [101] direction.

At deposition temperatures above 200 °C, the initial deposit consists of islands, and a greater mass thickness is required to reach continuous film formation. In addition to the formation of islands and films, nanowire growth and faceting are observed. For example, at 243 °C, a film grown for 109 min has nanowires that are 3.5  $\mu\text{m}$  long and 50 nm wide; these wires are thin enough to be technologically relevant for hydrogen-storage applications.

## CRedit authorship contribution statement

R. Joseph Lastowski: Writing – review & editing, Validation, Resources. **Jessica A. Krogstad**: Supervision. **John R. Abelson**: Writing – review & editing, Visualization, Validation, Supervision, Project administration, Funding acquisition, Conceptualization. **Samyukta Shrivastav**: Writing – review & editing, Resources, Investigation, Formal analysis. **Gregory S. Girolami**: Writing – review & editing, Validation, Supervision, Resources, Project administration, Funding acquisition, Conceptualization. **Laurent Souqui**: Writing – review & editing, Writing – original draft, Visualization, Validation, Project administration, Investigation, Formal analysis, Conceptualization. **Christopher M. Caroff**: Writing – original draft, Validation, Resources.

## Declaration of Competing Interest

The authors declare that they have no known competing financial interests or personal relationships that could have appeared to influence the work reported in this paper.

## Acknowledgements

This work was funded by NSF CMMI 18–25938 (to J.R.A.) and by NSF CHE 24–00099 (to G.S.G.). Materials characterization was carried out in part at the Materials Research Laboratory Central Research Facilities, University of Illinois. We thank Richard T. Haasch of the Materials Research Center at the University of Illinois for obtaining the XPS spectra.

## Appendix A. Supporting information

Supplementary data associated with this article can be found in the online version at [doi:10.1016/j.mtcomm.2025.114615](https://doi.org/10.1016/j.mtcomm.2025.114615).

## Data availability

Data will be made available on request.

## References

- [1] D. Moser, G. Baldissin, D.J. Bull, D.J. Riley, I. Morrison, D.K. Ross, W.A. Oates, D. Noréus, *J. Phys. Condens. Matter* 23 (2011), <https://doi.org/10.1088/0953-8984/23/30/305403>.
- [2] J. Isidorsson, M.E. Giebels, R. Griessen, H. Arwin, *Condens. Matter Mater. Phys. Phys. Rev. B* 68 (2003) 1.
- [3] M. Ismail, Y. Zhao, X.B. Yu, S.X. Dou, *Energy Educ. Sci. Technol. Part A Energy Sci. Res.* 30 (2012) 107.
- [4] M. Barawi, C. Granero, P. Díaz-Chao, C.V. Manzano, M. Martin-Gonzalez, D. Jimenez-Rey, I.J. Ferrer, J.R. Ares, J.F. Fernández, C. Sánchez, *Int. J. Hydrog. Energy* 39 (2014) 9865.
- [5] B. Sakintuna, F. Lamari-Darkrim, M. Hirscher, *Int. J. Hydrog. Energy* 32 (2007) 1121.
- [6] V. Bérubé, G. Radtke, M. Dresselhaus, C. Gang, *Int. J. Energy Res.* 31 (2007) 637.
- [7] X. Yao, G. Lu, *Chin. Sci. Bull.* 53 (2008) 2421.
- [8] J.C. Crivello, B. Dam, R.V. Denys, M. Dornheim, D.M. Grant, J. Huot, T.R. Jensen, P. de Jongh, M. Latroche, C. Milanese, D. Milčius, G.S. Walker, C.J. Webb, C. Zlotea, V.A. Yartys, *Appl. Phys. A Mater. Sci. Process* 122 (2016) 1.
- [9] T. Sadhasivam, H.T. Kim, S. Jung, S.H. Roh, J.H. Park, H.Y. Jung, *Renew. Sustain. Energy Rev.* 72 (2017) 523.
- [10] Y. Sun, C. Shen, Q. Lai, W. Liu, D.W. Wang, K.F. Aguey-Zinsou, *Energy Storage Mater.* 10 (2018) 168.
- [11] V.A. Yartys, M.V. Lototskyy, E. Akiba, R. Albert, V.E. Antonov, J.R. Ares, M. Baricco, N. Bourgeois, C.E. Buckley, J.M. Bellosta von Colbe, J.C. Crivello, F. Cuevas, R.V. Denys, M. Dornheim, M. Felderhoff, D.M. Grant, B.C. Hauback, T. D. Humphries, I. Jacob, T.R. Jensen, P.E. de Jongh, J.M. Joubert, M.A. Kuzovnikov, M. Latroche, M. Paskevicius, L. Pasquini, L. Popilevsky, V.M. Skripnyuk, E. Rabkin, M.V. Sofianos, A. Stuart, G. Walker, H. Wang, C.J. Webb, M. Zhu, *Int. J. Hydrog. Energy* 44 (2019) 7809.
- [12] Á. Révész, M. Gajdics, *Energies* 14 (2021), <https://doi.org/10.3390/en14196400>.
- [13] I.A.M.E. Giebels, J. Isidorsson, R. Griessen, *Condens. Matter Mater. Phys. Phys. Rev. B* 69 (2004) 1.
- [14] J. Karst, M. Hentschel, F. Sterl, H. Linnenbank, M. Ubl, H. Giessen, *Opt. Mater. Express* 10 (2020) 1346.
- [15] S.Z. Karazhanov, A.G. Ulyashin, P. Vajeeston, P. Ravindran, *Philos. Mag.* 88 (2008) 2461.
- [16] C. Platzer-Björkman, T. Mongstad, S. Karazhanov, J.P. Mæhlen, E. Marstein, A. Holt, *Mater. Res. Soc. Symp. Proc.* 1210 (2010) 1.
- [17] C. Platzer-Björkman, T. Mongstad, J.P. Mæhlen, A. Baldi, S. Karazhanov, A. Holt, *Thin Solid Films* 519 (2011) 5949.
- [18] E. Wiberg, R. Bauer, *Chem. Ber.* 85 (1952) 593.
- [19] Y. Chen, J. Williams, *Mater. Sci. Forum* 225–227 (1996) 881.
- [20] R. Schulz, J. Huot, G.X. Liang, S. Boily, A. Van Neste, J. Metast. *Nanocrystall. Mater.* 2–6 (1999) 615.
- [21] J. Huot, G. Liang, S. Boily, A. Van Neste, R. Schulz, *J. Alloy. Compd.* 293 (1999) 495.
- [22] P. Wang, H.F. Zhang, B.Z. Ding, Z.Q. Hu, *J. Alloy. Compd.* 313 (2000) 209.
- [23] P. Wang, A.M. Wang, Y.L. Wang, H.F. Zhang, Z.Q. Hu, *Scr. Mater.* 43 (2000) 83.
- [24] J. Lyu, A. Lider, V. Kudiiarov, *Metals* 9 (2019), <https://doi.org/10.3390/met9070768>.
- [25] C. Zhou, Y. Peng, Q. Zhang, *J. Mater. Sci. Technol.* 50 (2020) 178.
- [26] A.F. Gross, C.C. Ahn, S.L. Van Atta, P. Liu, J.J. Vajo, *Nanotechnology* 20 (2009), <https://doi.org/10.1088/0957-4484/20/20/204005>.
- [27] T.K. Nielsen, K. Manickam, M. Hirscher, F. Besenbacher, T.R. Jensen, *ACS Nano* 3 (2009) 3521.
- [28] S. Zhang, A.F. Gross, S.L. Van Atta, M. Lopez, P. Liu, C.C. Ahn, J.J. Vajo, C. M. Jensen, *Nanotechnology* 20 (2009), <https://doi.org/10.1088/0957-4484/20/20/204027>.
- [29] P. Huen, M. Paskevicius, B. Richter, D.B. Ravnsbæk, T.R. Jensen, *Inorganics* 5 (2017) 1.
- [30] I. Saita, T. Tushima, S. Tanda, T. Akiyama, *Mater. Trans.* 47 (2006) 931.
- [31] C. Zhu, S. Hosokai, T. Akiyama, *Cryst. Growth Des.* 11 (2011) 4166.
- [32] K. Park, J. Han, *Korean J. Chem. Eng.* 29 (2012) 1336.
- [33] C. Zhu, S. Hosokai, T. Akiyama, *Int. J. Hydrog. Energy* 37 (2012) 8379.
- [34] T. Zhang, Y. Song, Z. Han, X. Chen, X. Zhao, S. Zhou, H. Yu, *Cryst. Res. Technol.* 53 (2018) 1.
- [35] R.J. Westerwaal, C.P. Broedersz, R. Gremaud, M. Slaman, A. Borgschulte, W. Lohstroh, K.G. Tschersich, H.P. Fleischhauer, B. Dam, R. Griessen, *Thin Solid Films* 516 (2008) 4351.
- [36] H. Le-Quoc, A. Lacoste, S. Miraglia, S. Béchu, A. Bès, L. Laversenne, *Int. J. Hydrog. Energy* 39 (2014) 17718.
- [37] R. Shimizu, T. Kakinokizono, I. Gu, T. Hitosugi, *Inorg. Chem.* 58 (2019) 15354.
- [38] J.R. Abelson, G.S. Girolami, *J. Vac. Sci. Technol. A* 38 (2020) 030802.
- [39] W. Pyka, C. Heitzinger, N. Tamaoki, T. Takase, T. Ohmine, S. Selberherr, *Proc. Int. Conf. Simul. Semicond. Devices Process. SISPAD* (2001) 124–127.
- [40] N. Kumar, a Yanguas-Gil, S.R. Daly, G.S. Girolami, J.R. Abelson, *J. Am. Chem. Soc.* 130 (2008) 17660.
- [41] A. Yanguas-Gil, Y. Yang, N. Kumar, J.R. Abelson, *J. Vac. Sci. Technol. A Vac. Surf. Film.* 27 (2009) 1235.
- [42] A. Yanguas-Gil, N. Kumar, Y. Yang, J.R. Abelson, *J. Vac. Sci. Technol. A Vac. Surf. Film.* 27 (2009) 1244.
- [43] J.R. Abelson, *ECS Trans.* 33 (2010) 307.
- [44] W.B. Wang, N.N. Chang, T.A. Coddling, G.S. Girolami, J.R. Abelson, *J. Vac. Sci. Technol. A Vac. Surf. Film.* 32 (2014) 051512.
- [45] Y. Huang, Y. Cheng, J. Zhang, *Ind. Eng. Chem. Res.* 60 (2021) 2737.
- [46] C.M. Caroff, Ph.D. Thesis, University of Illinois, Aminodiboranates Diaminodiboranates Dialkyltriazinides Synth. Struct. Appl. Chem. Vap. Depos. (2023).
- [47] Z. Zhang, Ph.D. Thesis, University of Illinois, Nucleic Inhib. Enhanc. Chem. Vap. Depos. (2020).
- [48] S. Jayaraman, Y. Yang, D.Y. Kim, G.S. Girolami, J.R. Abelson, *J. Vac. Sci. Technol. A Vac. Surf. Film.* 23 (2005) 1619.
- [49] S. Jayaraman, J.E. Gerbi, Y. Yang, D.Y. Kim, A. Chatterjee, P. Bellon, G.S. Girolami, J.P. Chevalier, J.R. Abelson, *Surf. Coat. Technol.* 200 (2006) 6629.
- [50] A. Yanguas-Gil, B.A. Sperling, J.R. Abelson, *Phys. Rev. B Condens. Matter Mater. Phys.* 84 (2011) 1.
- [51] X. Wang, Z. Guo, Y. Gao, J. Wang, *J. Mater. Res.* 32 (2017) 37.
- [52] J. Santisteban, G. Cuello, J. Dawidowski, A. Fainstein, H. Peretti, A. Ivanov, *Condens. Matter Mater. Phys. Phys. Rev. B* 62 (2000) 37.
- [53] L. Matović, N. Novaković, S. Kurko, M. Šiljegović, B. Matović, Z. Kačarević Popović, N. Romčević, N. Ivanović, J. Grbović Novaković, *Int. J. Hydrog. Energy* 34 (2009) 7275.
- [54] M.A. Kuzovnikov, V.S. Efimchenko, E.V. Filatov, A.A. Maksimov, I.I. Tartakovskii, A.J. Ramirez-Cuesta, *Solid State Commun.* 154 (2013) 77.
- [55] C.H.J. Van den Brekel, A.K. Jansen, *J. Cryst. Growth* 43 (1978) 364.
- [56] B.J. Palmer, R.G. Gordon, *Thin Solid Films* 177 (1989) 141.
- [57] G. Bales, A. Redfield, A. Zangwill, *Phys. Rev. Lett.* 62 (1989) 776.
- [58] M. Law, J. Goldberger, P. Yang, *Annu. Rev. Mater. Res.* 34 (2004) 83.
- [59] A. Colli, A. Fasoli, S. Hofmann, C. Ducati, J. Robertson, A.C. Ferrari, *Nanotechnology* 17 (2006) 1046.
- [60] D.L. Ma, H.L. Chen, *J. Cryst. Growth* 335 (2011) 127.
- [61] C.J. Hawley, B.R. Beatty, G. Chen, J.E. Spanier, *Cryst. Growth Des.* 12 (2012) 2789.
- [62] T.T. Xu, J.G. Zheng, N. Wu, A.W. Nicholls, J.R. Roth, D.A. Dikin, R.S. Ruoff, *Nano Lett.* 4 (2004) 963.
- [63] Zheng Wei Pan, Zu Rong Dai, Zhong Lin Wang, *Science* 291 (2001) 1947.
- [64] W. Wu, Q. Yu, J. Lian, J. Bao, Z. Liu, S.S. Pei, *J. Cryst. Growth* 312 (2010) 3147.
- [65] S. Mihai, D.L. Cursaru, D. Matei, A.M. Manta, R. Somoghi, G. Branouiu, *Sci. Rep.* 9 (2019) 1.
- [66] C. Zhu, N. Sakaguchi, S. Hosokai, S. Watanabe, T. Akiyama, *Int. J. Hydrog. Energy* 36 (2011) 3600.

- [67] A. Surrey, L. Schultz, B. Rellinghaus, *Adv. Struct. Chem. Imaging* 2 (1) (2016).
- [68] W. Li, C. Li, H. Ma, J. Chen, *J. Am. Chem. Soc.* 129 (2007) 6710.
- [69] J.J. Liang, *Appl. Phys. A Mater. Sci. Process* 80 (2005) 173.
- [70] B. Peng, L. Li, W. Ji, F. Cheng, J. Chen, *J. Alloy. Compd.* 484 (2009) 308.
- [71] H. Richter, Z.P. Wang, L. Ley, *Solid State Commun.* 39 (1981) 625.
- [72] F. Cerdeira, C.J. Buchenauer, F.H. Pollak, M. Cardona, *Phys. Rev. B* 5 (1972) 580.
- [73] F.H. Ellinger, C.E. Holley, B.B. McInTeer, D. Pavone, R.M. Potter, E. Staritzky, W. H. Zachariasen, *J. Am. Chem. Soc.* 77 (1955) 2647.
- [74] C. Weidenthaler, *Nanoscale* 3 (2011) 792.
- [75] D. Simeone, G. Baldinozzi, D. Gosset, S. Le Caer, J.F. Bérrar, *Thin Solid Films* 530 (2013) 9.
- [76] W.A. Dollase, *J. Appl. Crystallogr.* 19 (1986) 267.
- [77] E. Zolotoyabko, *J. Appl. Crystallogr.* 42 (2009) 513.
- [78] J.J. Tang, X.B. Yang, L.J. Chen, Y.J. Zhao, *AIP Adv.* 4 (2014), <https://doi.org/10.1063/1.4886384>.
- [79] W.Y. Chen, J.J. Tang, Z.W. Lu, M.X. Huang, L. Liu, C.C. He, Y.J. Zhao, *Surf. Sci.* 710 (2021) 121850.
- [80] Y. Zhang, J. Wu, M. Aagesen, H. Liu, *J. Phys. D. Appl. Phys.* 48 (2015), <https://doi.org/10.1088/0022-3727/48/46/463001>.
- [81] L. Güniat, P. Caroff, A. Fontcuberta, I. Morral, *Chem. Rev.* 119 (2019) 8958.
- [82] P.C. McIntyre, A. Fontcuberta i Morral, *Mater. Today Nano* 9 (2020) 100058.
- [83] D. Milcius, J. Grbović-Novaković, R. Zostautiene, M. Lelis, D. Girdzevicius, M. Urbonavicius, *J. Alloy. Compd.* 647 (2015) 790.
- [84] X. Zhang, Y. Liu, Z. Ren, X. Zhang, J. Hu, Z. Huang, Y. Lu, M. Gao, H. Pan, *Energy Environ. Sci.* 14 (2021) 2302.
- [85] J.F. Ziegler, W.K. Chu, *At. Data Nucl. Data Tables* 13 (1974) 463.
- [86] M. Mayer, *Nucl. Instrum. Methods Phys. Res. Sect. B Beam Interact. with Mater. Atoms* 2002, 194, 177.
- [87] R. Grau-Crespo, K.C. Smith, T.S. Fisher, N.H. de Leeuw, U.V. Waghmare, *Phys. Rev. B* 80 (2009) 174117.
- [88] L. Bao, J. Shi, Q. Le, *Crystals* 14 (2024) 750.
- [89] R.E. Stephens, I.H. Malitson, *J. Res. Natl. Bur. Stand* 49 (1952) 249 (1934).
- [90] R.A. Synowicki, T.E. Tiwald, *Thin Solid Films* 455–456 (2004) 248.
- [91] Q. Ren, Q. Luo, Y. Hou, *Adv. Mater. Res.* 412 (2012) 427.
- [92] P.C. Keller, H.D. Johnson, *Inorg. Synth.* (1977) 30–32.
- [93] P.C. Keller, G.E. Ryschkewitsch, *Inorg. Chem.* 1977, pp. 32–34..
- [94] C.M. Caroff, G.S. Girolami, *Inorg. Chem.* 62 (2023) 3116.
- [95] M. Dai, G. Lei, Z. Zhang, Z. Li, H. Cao, P. Chen, *Acta Chim. Sin.* 80 (2022) 303.